Title

In vivo imaging reveals transient microglia recruitment and functional recovery of photoreceptor signaling after injury.

Journal

Proceedings of the National Academy of Sciences of the United States of America, 116(33)

ISSN

0027-8424

Authors

Miller, Eric B
Zhang, Pengfei
Ching, Karli
et al.

Publication Date

2019-08-01

DOI

10.1073/pnas.1903336116

Peer reviewed

In vivo imaging reveals transient microglia recruitment and functional recovery of photoreceptor signaling after injury

Eric B. Miller[a], Pengfei Zhang[b], Karli Ching[a], Edward N. Pugh Jr[b,c,d], and Marie E. Burns[a,b,c,1]

[a]Center for Neuroscience, University of California, Davis, CA 95616; [b]Department of Cell Biology and Human Anatomy, University of California, Davis, CA 95616; [c]Department of Ophthalmology & Vision Science, University of California, Davis, CA 95616; and [d]Department of Physiology and Membrane Biology, University of California, Davis, CA 95616

Edited by Jeremy Nathans, Johns Hopkins University, Baltimore, MD, and approved June 25, 2019 (received for review February 25, 2019)

Microglia respond to damage and microenvironmental changes within the central nervous system by morphologically transforming and migrating to the lesion, but the real-time behavior of populations of these resident immune cells and the neurons they support have seldom been observed simultaneously. Here, we have used in vivo high-resolution optical coherence tomography (OCT) and scanning laser ophthalmoscopy with and without adaptive optics to quantify the 3D distribution and dynamics of microglia in the living retina before and after local damage to photoreceptors. Following photoreceptor injury, microglia migrated both laterally and vertically through the retina over many hours, forming a tight cluster within the area of visible damage that resolved over 2 wk. In vivo OCT optophysiological assessment revealed that the photoreceptors occupying the damaged region lost all light-driven signaling during the period of microglia recruitment. Remarkably, photoreceptors recovered function to near-baseline levels after the microglia had departed the injury locus. These results demonstrate the spatiotemporal dynamics of microglia engagement and restoration of neuronal function during tissue remodeling and highlight the need for mechanistic studies that consider the temporal and structural dynamics of neuron–microglia interactions in vivo.

retina | microglia | photoreceptor | laser | imaging

Microglia are resident immune cells of the central nervous system (CNS) that constantly monitor the microenvironment of the neural parenchyma (1, 2) participating in synaptic pruning during development and in synaptic maintenance in adulthood (1). In response to neuronal damage or degeneration, microglia become activated, morphing into an "ameboid" form that can migrate to sites of injury where they phagocytose debris and dying cells (3). Activated microglia can also signal to neuroglia and circulating monocytes, triggering inflammation and exacerbating neurodegenerative disease (4, 5). Because microglia are highly dynamic in both form and function, it is critical to study them within their native milieu over time and to assess the functionality of the neurons within the microenvironments they support.

The retina is CNS tissue whose large microglial population can be imaged noninvasively and longitudinally through the eye's natural optics (6–17). In this investigation, we have taken advantage of recent advances in mouse retinal imaging, applying scanning laser ophthalmoscopy (SLO) and adaptive optics SLO (AO-SLO) imaging in vivo to assess entire populations of microglia at high spatial resolution in *Cx3CR1*$^{+/GFP}$ and *Cx3CR1*$^{GFP/GFP}$ mice. By simultaneously applying optical coherence tomography (OCT) to extract the 3D retinal architecture, we surveyed microglia within the same, aligned retinal volume over time periods ranging from seconds to months, comparing their motility in their resting state to that during their transient response to a small (~150 μm in diameter) focal injury of photoreceptors. Furthermore, by optically assessing photoreceptor density and function both within and outside the region of damage over many weeks, we quantified in vivo the neuronal degeneration, repair, and remodeling that took place in relation to the microglia spatiotemporal dynamics.

Results

Baseline Morphology, Densities, and Dynamics of Microglia in the Healthy Retina In Vivo. To create a baseline for investigating changes in microglia induced by neuronal injury in vivo, we first characterized key features of large microglial populations in retinas of *Cx3CR1*$^{+/GFP}$ and *Cx3CR1*$^{GFP/GFP}$ mice, including their spatial density, their distribution in different retinal layers and their branch morphology and motility. We employed simultaneous OCT and SLO fluorescence imaging, a multimodal approach that enables alignment of widefield SLO images with *en face* OCT projections of the retina's vitreal surface, using the major retinal vessels as landmarks (Fig. 1*A*). As a consequence, microglia were precisely localized on a stable vascular map that could be enlarged to cover an even greater field of view by stitching together images taken after moving the scan optic axis (*SI Appendix*, Fig. S1 *A–D*). The resultant retinal maps, which covered ~5 mm^2 per eye, had microglial densities in good agreement with previous measurements (8, 9, 12, 18), while also revealing subtle but reliable differences in microglia populations and spatial distributions between *Cx3CR1*$^{+/GFP}$ and *Cx3CR1*$^{GFP/GFP}$ mice (*SI Appendix*, Fig. S1 *E–H*). We observed an overall increase in the number of retinal microglia in

Significance

Microglia, the resident macrophages of the central nervous system, are critical for synaptic pruning and maintenance and for mitigating injury and neurodegeneration. Determining whether microglia–neuron interactions are beneficial in specific instances has been difficult, largely because of the local and transient nature of the interactions. Using simultaneous optical coherence tomography/scanning laser ophthalmoscopy (SLO) and adaptive optics SLO retinal imaging in mice, we show interactions of microglia and photoreceptors over time scales from seconds to months during injury, degeneration, and repair. In vivo optical assessment of photoreceptor signaling in a large neuronal field encompassing the injured area allows us to relate the time course of these microglia movements to that of the tissue remodeling and functional recovery.

Author contributions: E.B.M., E.N.P., and M.E.B. designed research; E.B.M., P.Z., and K.C. performed research; P.Z. contributed new reagents/analytic tools; E.B.M., K.C., and M.E.B. analyzed data; and E.B.M., E.N.P., and M.E.B. wrote the paper.

The authors declare no conflict of interest.

This article is a PNAS Direct Submission.

[1]To whom correspondence may be addressed. Email: meburns@ucdavis.edu.

This article contains supporting information online at www.pnas.org/lookup/suppl/doi:10.1073/pnas.1903336116/-/DCSupplemental.

Published online July 26, 2019.

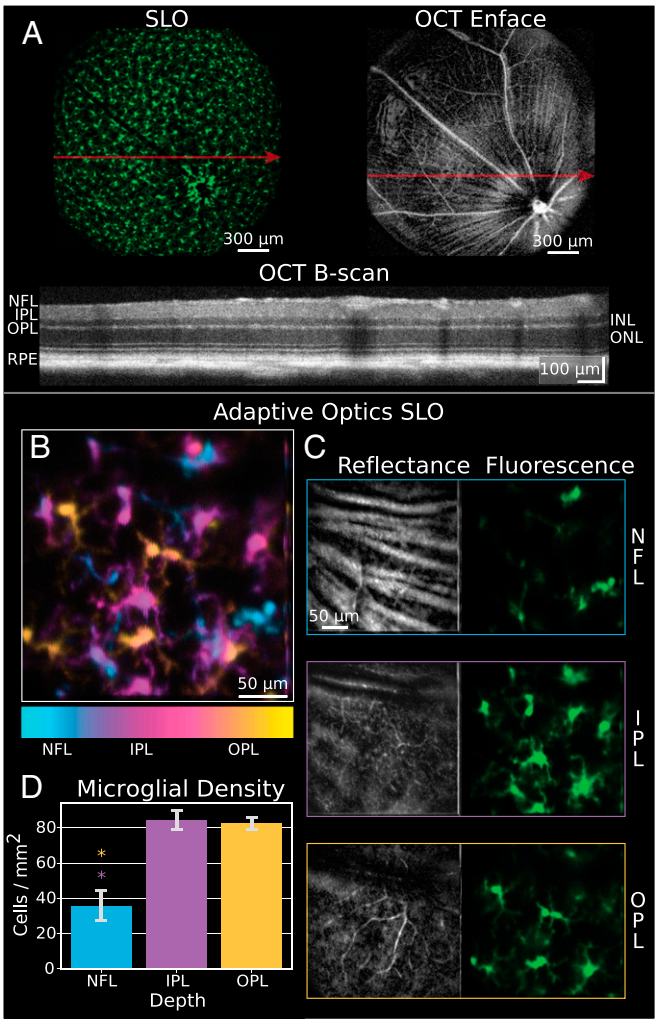

Fig. 1. Wide-field and depth-layer distribution of microglia in the living retina with adaptive optics. (*A*) Simultaneous wide-field SLO fluorescence and *en face* OCT imaging of the retina of *Cx3Cr1*$^{+/GFP}$ mice give aligned views of the microglia (green) and the vasculature of the retinal surface. The OCT B-scan in *A* was taken at the position indicated by the light blue arrow. The retinal area imaged has an area of ∼3.2 mm^2. (*B*) AO-SLO image of retinal microglia of a *Cx3CR1*$^{+/GFP}$ mouse, with microglia color-coded for depth. (*C*) The unique OCT scattering patterns of ganglion cell axon bundles and the retinal vasculature serve as spatial reference maps for the localization of microglia in 3 dimensions, yielding coregistered reflectance and fluorescence images. (*D*) Quantification of cell density in NFL, IPL, and OPL, measured at multiple locations ∼750 μm from the ONH. NFL vs. IPL *t* test $P = 7.45 \times 10^{-5}$, NFL vs. OPL *t* test $P = 3.5 \times 10^{-5}$, IPL vs. OPL *t* test $P = 0.77$. *$P <$ 0.0001. NFL, nerve fiber layer; IPL, inner plexiform layer; OPL, outer plexiform layer; ONH, optic nerve head (see also Movie S1).

mice lacking Cx3CR1 expression (*Cx3CR1*$^{GFP/GFP}$ vs. *Cx3CR1*$^{+/GFP}$), with green fluorescent protein-positive (GFP+) cells being particularly dense in the central retinal (*SI Appendix*, Fig. S1 *E–H*). Similar increases in microglia number have been noted recently in adult *Cx3CR1*$^{GFP/GFP}$ mice compared with wild-type controls (19). For these reasons, we limited our further investigations to *Cx3CR1*$^{+/GFP}$ mice unless otherwise indicated.

To examine the morphology and distribution of microglia in different retinal layers in in vivo, we employed AO-SLO confocal imaging. AO-SLO corrects the optical aberrations across the aperture of the dilated pupil, enabling optimum use of the mouse eye's ∼0.5 numerical aperture so that, unlike with conventional SLO, the different retinal layers can be resolved (6, 17, 20) (Movie S1). AO-SLO imaging of *Cx3CR1*$^{+/GFP}$ mice revealed distinct populations of cells within the retinal layers (Fig. 1*B*), with cells in the nerve fiber layer (NFL) appearing far less ramified than those in the synaptic, plexiform layers (Fig. 1*C*). Furthermore the branches of the microglia in the outer plexiform layer (OPL) appeared to be nearly planar, while the microglia in the inner plexiform layer (IPL) appeared more pyramidal (Movie S1), likely because the OPL is structurally thinner (20 μm vs. 60 μm for ONL and INL, respectively) (21). The density of microglia in the synaptic layers (IPL and OPL; Fig. 1*C*) was more than twice that of the fiber layer, but there was no detectable difference in the densities in the IPL and OPL (*F* test result: 20.69, $P = 1.5 \times 10^{-6}$, NFL vs. IPL *t* test $P = 7.45 \times 10^{-5}$, NFL vs. OPL *t* test $P = 3.5 \times 10^{-5}$, IPL vs. OPL *t* test $P = 0.77$; Fig. 1*D*). These results support the hypothesis that the normal function of branched "resting microglia" is synaptic maintenance (22). In vivo time-lapse imaging revealed the branches of ramified microglia in healthy retina to be mostly stationary over the time scale of minutes (*SI Appendix*, Fig. S2 *A* and *B*, green boxes and arrows). In contrast, less abundant nonramified "ameboid" cells showed rapid movements of "ball and chain"-like structures or beating "fin"-like protuberances (*SI Appendix*, Fig. S2 *A* and *B*, red and cyan boxes and arrows and Movies S2–S5). We note that although the vast majority of GFP+ cells in the healthy retina are expected to be microglia, monocytes and bone marrow-derived macrophages also express Cx3CR1 and thus may also be represented in the GFP+ population of cells.

Spatial Extent and Dynamics of the Microglial Response to Injury of a Small Population of Photoreceptors. Having determined the characteristics of the microglia population of the normal retina in vivo, we examined the changes they undergo in response to cellular damage caused by a focal near-infrared (NIR) laser irradiation (Fig. 2 and *SI Appendix*, Figs. S2 *C–G* and S3). Multimodal mapping with SLO and OCT enabled reliable reexamination of the injury locus over 3 mo and of the microglial response in a large field encompassing the injury. Immediately after laser exposure, OCT volume scans revealed a region in the outer retina ∼150 μm in diameter with greatly increased scattering (Fig. 2, Post and *SI Appendix*, Fig. S3*A*), indicative of neuronal damage (23–28). The lateral extent of the increased scattering defined an "injury field," whose confinement between the OPL and the retinal pigment epithelium (RPE) (Fig. 2, *SI Appendix*, Fig. S3*A* and Movies S6–S9) established the volume of damaged tissue to be predominantly photoreceptors. Time-lapse, high-resolution SLO imaging of the microglia within and surrounding the injury field showed no detectable mobilization or activation of microglia up to 1 h after irradiation (*SI Appendix*, Fig. S2 *C–G*). However, at later times there was an apparent decrease in the amount of microglia in an area surrounding the injury field. This suggests that the local microglia in the "response field" migrate to the injury field. The greatest decrease in microglia in the response field was at 2 d postdamage but returned nearly to baseline by 21 d (*SI Appendix*, Fig. S3*C*). Both the degree of photoreceptor damage revealed by the OCT light scattering and the accumulation of microglia at the injury locus revealed by the SLO fluorescence intensity reached maxima ∼2 d after the injury and declined gradually thereafter, returning close to the preinjury baselines by 21 d (Fig. 2, orange boxes and *SI Appendix*, Fig. S3). These results show that the NIR laser exposure, while sufficient to damage photoreceptors to the extent that they activated microglia, was nonetheless moderate enough to permit tissue remodeling and return to homeostasis.

Microglia Transform to a Distinctly Polarized Form as They Migrate Laterally and in Depth to the Injury Locus. To more completely resolve the time course and spatial extent of microglial recruitment to the injury locus, we repeated the experiment, performing high-resolution SLO/OCT and AO-SLO imaging at various

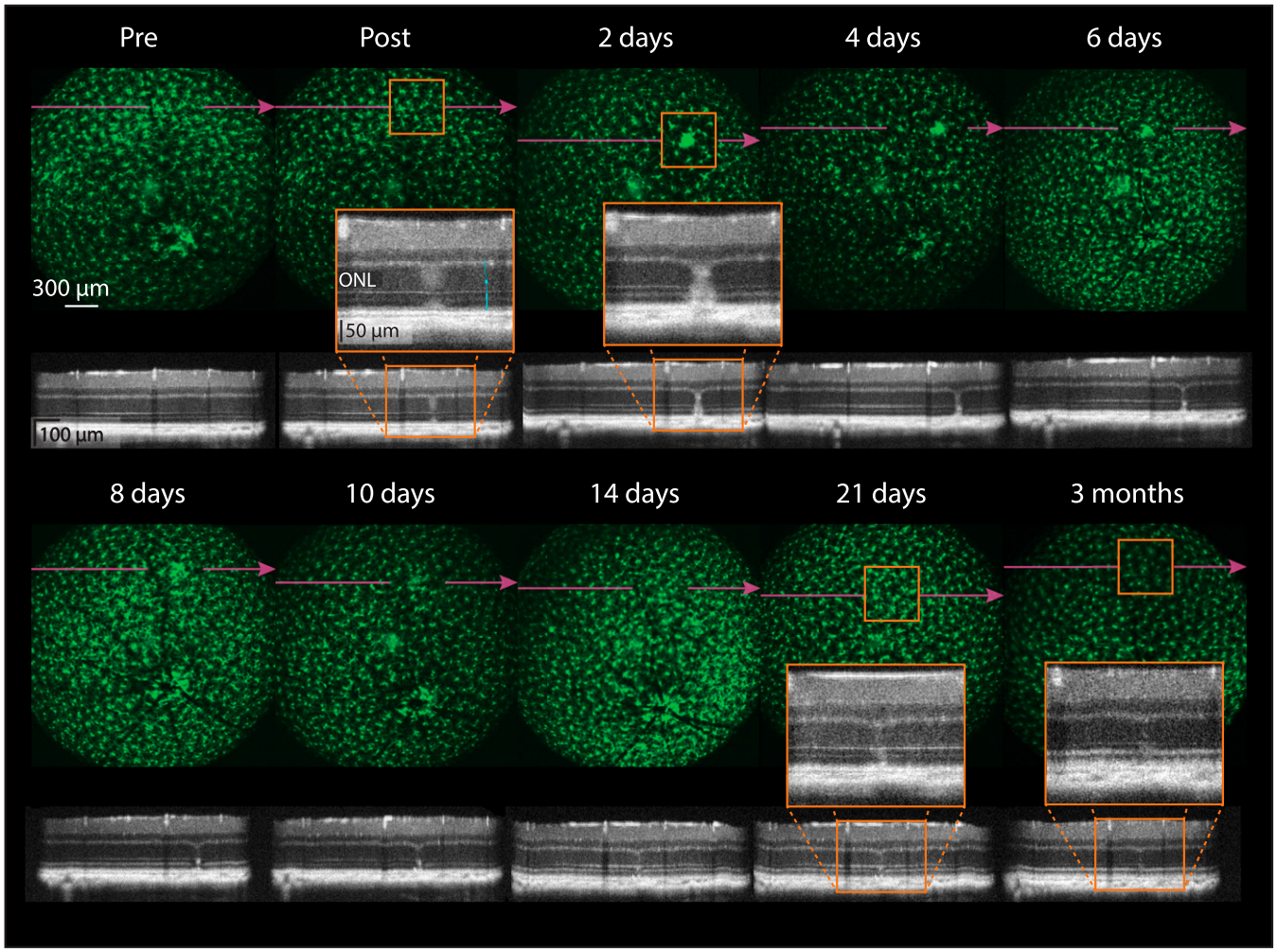

Fig. 2. Long-term, wide-field multimodal SLO and OCT imaging reveals the time course of microglia response and tissue remodeling after a focal injury. SLO (wide-field images, GFP fluorescence shown in green) and OCT imaging of the same mouse retina over a period of 3 mo before (Pre), immediately after (Post) and on standard time points up to 3 mo after focal injury by an NIR laser exposure. The locus of the injury is revealed both by increased OCT scattering immediately after the injury and by continued increased scattering in the ONL (inset orange boxes), by and concomitant congregation of microglia at the injury locus on day 2. By 21 d the microglia had reestablished a normal distribution and the increased OCT scattering had largely abated.

subsequent intervals over the initial 24 h after NIR laser exposure (Fig. 3 and *SI Appendix*, Figs. S4–S9). OCT showed that the NIR irradiation increased scattering in the photoreceptor nuclear layer (ONL) immediately after the exposure (0 h). This "injury field" expanded over the ensuing hours and included disruption of the external limiting membrane (ELM) and diminished scattering in the RPE layer by 16 h, suggesting secondary damage to these structures (Fig. 3*A*, OCT column). Application of the "superaveraging" OCT protocol of Liu et al. (29) to improve resolution revealed highly structured scattering elements in the undamaged ONL, which appear to correspond to photoreceptor cell bodies (Fig. 3*A*, OCT and Merge columns and Movies S6–S10). In the injury field, similarly shaped scattering elements were present, but the axial spacing was disrupted and many of the putative cell bodies had highly increased scattering relative to the corresponding elements in the control region (Movies S6–S9). By 8 h, the damaged region was less uniform in its light-scattering properties, with distinct bright puncta amid what appeared to be unstructured "black holes," which seemed to grow more severe by 24 h (e.g., Movie S9, frame 236). These latter may correspond to areas identified histologically as activated microglia and missing photoreceptor somata, as described below (Fig. 4).

SLO fluorescence imaging collected simultaneously with the OCT scanning revealed that GFP+ cell bodies had entered the injury field by 8 h (Fig. 3*A* and *SI Appendix*, Fig. S4, SLO column). Over the course of 24 h, a larger field of microglia surrounding the injury locus became highly polarized, with most branches oriented toward the injury rather than randomly distributed as in the neighboring healthy retina (*SI Appendix*, Fig. S4*A*, SLO). As the density of GFP+ somata within the injury locus increased, the response field darkened, consistent with the lateral migration of microglia into the injury field. Superposition of the OCT scans through the ONL injury field with the SLO GFP fluorescence images bounding the response field reveals the progression of photoreceptor injury and corresponding microglial response over time (Fig. 3*A*, Merge). Quantification of the injury and response fields across a population of animals revealed that on average the injury in the outer nuclear layer subtended a retinal area ~150 µm in diameter, while the microglia cluster at these early times was somewhat smaller, ~75 µm in radius increasing in cluster size and intensity progressively over 24 h ($n = 8$ retinas; *SI Appendix*, Fig. S4 *B–D*). Because the mice were awake and behaving over the course of the study except during the few brief imaging sessions, the slowness of the microglial response cannot be attributed to anesthesia but rather likely reflects retardation in migration through a relatively intact and dense parenchyma.

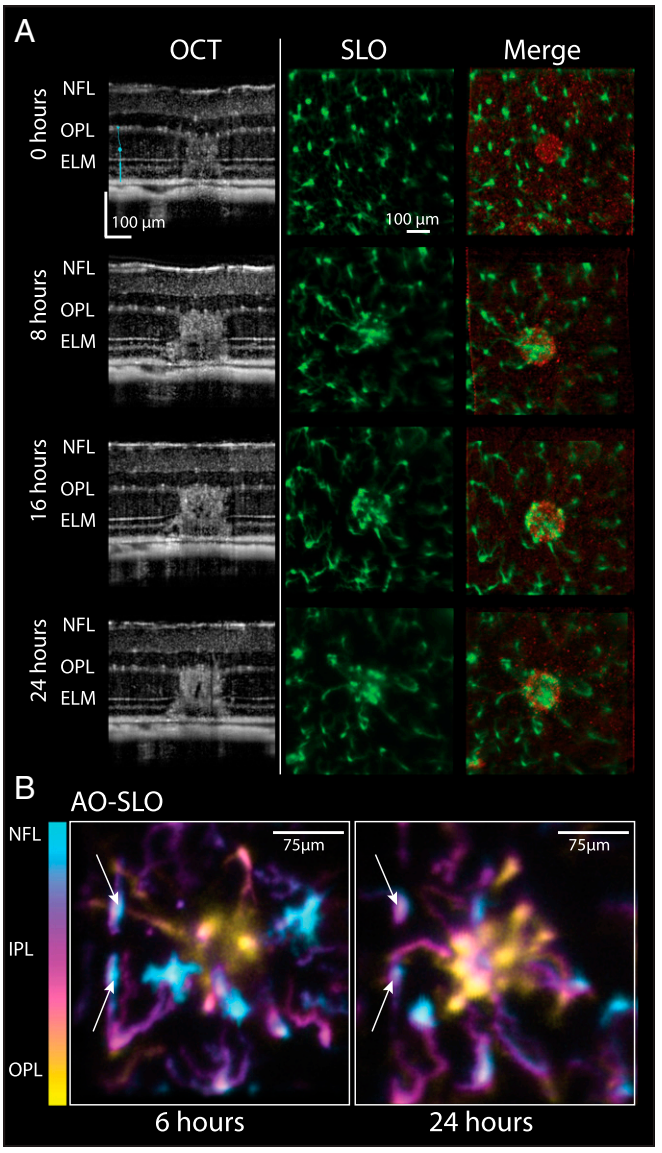

Fig. 3. Three-dimensional migration of microglia to the injured photoreceptor layer over 24 h revealed by AO-SLO. (*A*) Simultaneous high-resolution OCT and SLO in the first 24 h after focal damage reveal many details of the injury and microglia response in an individual mouse. By 8 h the injury field had widened, with disruption of the ELM, increased scattering throughout the photoreceptor layer, and decreased scattering by the RPE; the processes of most of the microglia in the 300-µm field exhibited polarization toward the injury. Microglia progressively migrated to the injury field at 16 and 24 h (SLO and Merge). Microglia density was highest within the area that had increased backscatter in the en-face OCT image (red channel, Merge). (*B*) AO-SLO images of microglia at damage location at 6 and 24 h after damage. OPL microglia cluster by 6 h, while the more superficial microglia are only beginning to undergo morphological changes. At 24 h, all OPL cells are inside the injury field, and there are fewer cells in the superficial retina. Superficial cells are in different locations at 6 and 24 h, indicating that superficial cells have migrated. All cells outside the injury field are highly polarized toward it. White arrows highlight GFP+ cells adjacent to a superficial retinal vessel that did not move over this time interval and may be perivascular macrophages.

Using AO-SLO we also assessed the vertical migration of microglia through the retinal layers (Fig. 3*B*). By 6 h, microglia in the photoreceptor synaptic layer (OPL) within the injury field had abandoned their baseline mosaic and were clustered at the center of the injury (yellow; compare Figs. 1*B* and Fig. 3*B*, 6 h). Microglia in the IPL (blue) and NFL (purple) remained stratified at this time but had undergone morphological changes, revealing that activating signals from the injured photoreceptors had reached the innermost retina by 6 h. After 24 h, almost all microglia in the response field had migrated and/or oriented toward the damage zone (Fig. 3*B*, 24 h). Only 2 cells in the 301-µm-wide AO-SLO image field did not move (Fig. 3*B*, arrows); these cells were apposite to a retinal vessel and therefore may have been perivascular macrophages that were unresponsive to the damage signal, or otherwise blocked from receiving it.

Persistent Gliosis and Microglia Recovery Accompany Tissue Remodeling. To confirm and further assess the extent of the cellular damage produced by the NIR irradiation, we examined retinal structure in the injury and response fields with histology. Plastic sections of retinas fixed 24 h after injury showed severe disruption of inner and outer segments (Fig. 4*A*, Plastic Section), confirming that the elevated OCT scattering within the column of ONL and OS/IS layers within the injury field reflected injury to photoreceptors (Fig. 4*B*, OCT B-scan). Immunohistochemistry of retinal flatmounts stained for CD11b, which is expressed in microglia and leukocytes, showed a small amount of CD11b+ cell infiltration into the injury field of the ONL 8 h after injury (Fig. 4*B*), consistent with the in vivo SLO imaging. DAPI staining within the ONL revealed a disrupted pattern and density of photoreceptor nuclei within the damaged region (Fig. 4 *B*, *Bottom Insets*), many of which were surrounded by CD11b+ cells (Fig. 4 *B*, *Top Inset* and Movie S11). The number of photoreceptor nuclei enclosed by CD11b+ cells increased over the first 24 h, consistent with a specific response of the immune cells to the injured photoreceptors (Fig. 4 and *SI Appendix*, Fig. S5).

Photoreceptor damage is often associated with gliotic changes in Müller cells, the radial neuroglia of the retina. Immunostaining for glial fibrillary acidic protein (GFAP), up-regulated during gliosis, was low 8 h after injury, but by 24 h cells expressing high levels of GFAP formed a perimeter around the injury field, while staining was not detectable in the damaged area itself at 24 h (Fig. 4*B*, 24 h). By 21 d, GFAP expression remained elevated in the area of the injury and was particularly high at its center, as if the hole created by the cleared photoreceptors had been cinched closed during the formation of a gliotic scar. No CD11b+ cell bodies were visible in the ONL at this time, although the cell directly over the core of the damage extended a single process from the OPL into the ONL. Instead of a persistent change, a mosaic of CD11b+ cells with normal morphology had reappeared in the OPL (Fig. 4*B*, 21 d), consistent with the imaging results showing the return to the baseline distribution of microglia. Remarkably, by 21 d photoreceptor somata had repopulated the scarred area at near-normal cell density (Fig. 4*B*, inset red box).

Photoreceptors in the Remodeled Injury Field Respond Normally to Light. To assess whether the photoreceptors in the remodeled damage zone were functional, we employed an optophysiological experimental protocol that measures rod phototransduction (30) (Fig. 5). The experiment briefly exposed a large region of the dark-adapted retina encompassing the injury zone to 488-nm light that isomerized 10% of the rhodopsin in rods and used OCT to follow phototransduction-induced changes in backscattering from different retinal layers. The bleaching-induced changes in OCT signaling are readily visualized by "difference images" that display the pixel-by-pixel numerical subtraction of the B-scans taken before and 150 s after the bleaching exposure (Fig. 5*A*). A control region ~400 µm outside the injury zone exhibited a normal optophysiological responses at all time points during the 21-d experiment, with strong scattering changes at the inner segment/outer segment junction (IS/OS) and the distal tips of the rod (Fig. 5*A*, Ctrl dashed box and Fig. 5 *B* and *C*, Control), as shown previously (30). Within

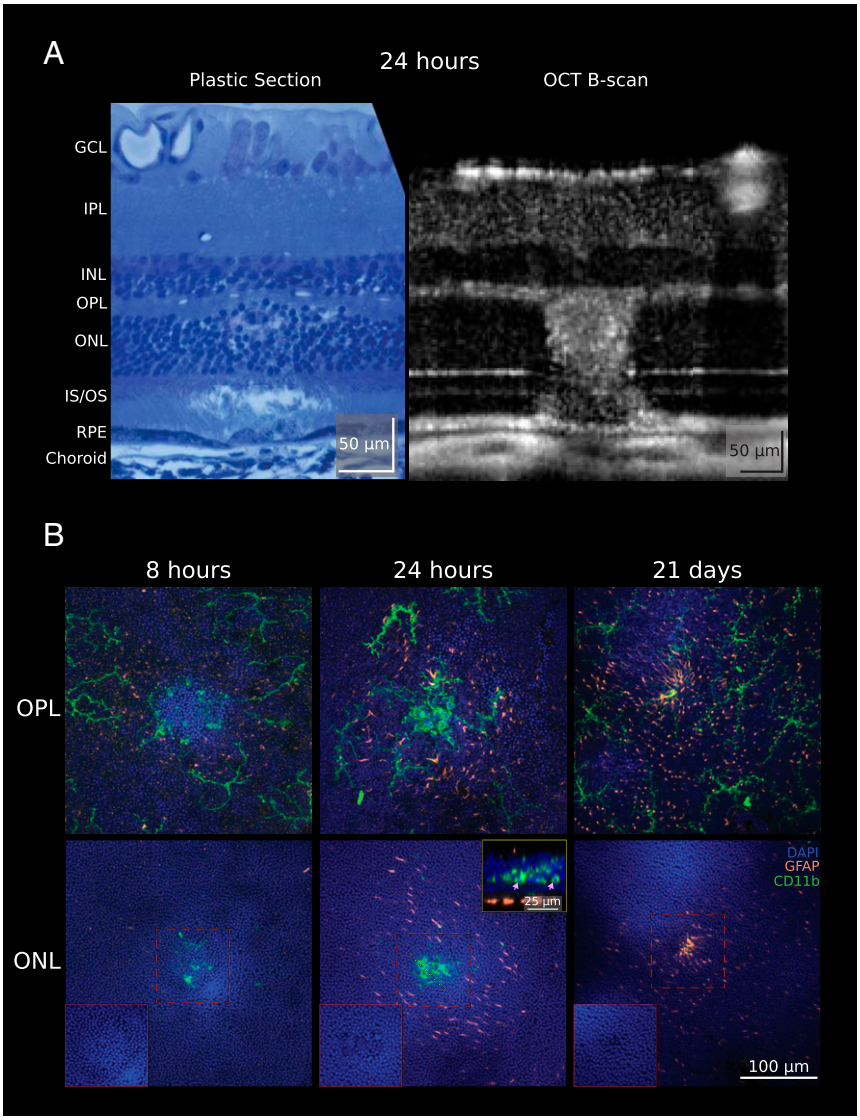

Fig. 4. Histological evidence of photoreceptor damage and remodeling and the pattern of glia and microglia responses. (*A*) Comparison of a toluidine blue-stained plastic section at an injury locus and "superaveraging" OCT B-scan, both 24 h after laser exposure from two different retinas. Green: immunostaining for CD11b, a microglial marker. Orange: staining for GFAP, a marker of Müller cells. Blue: DAPI, marking all cell nuclei. The pattern of ONL disruption and immunofluorescence strongly confirms the conclusions drawn from the in vivo observations of Figs. 2 and 3. (*B*) Confocal images (2 μm thick) of immunostained flatmounts of laser-damaged retinas after injury. Microglia (CD11b, green) in the OPL largely reestablished their normal distribution and vacated the ONL by 21 d. Increased GFAP expression (orange) in Müller glia was evident in the area surrounding the injury, but not its center, by 24 h. (*Top Right Inset*) Cross-section of image at location denoted by dashed yellow line shows microglia concentrated in the ONL. Pink arrowheads indicate DAPI+ nuclei surrounded by microglial processes. At 21 d, GFAP expression persisted and was concentrated at the center of the injury field where the photoreceptor somata had largely reestablished their normal distribution (*Bottom Left Insets*). Higher magnification of dashed red boxes, DAPI only.

the injury field at 8 h after the damaging NIR exposure, the OCT backscatter in the ONL and OS layers was broad and disrupted, with no reliable bleach-driven changes (red vs. blue, Fig. 5*B*, Injury Field, 8 h). The core of the injury field (inner ∼40-μm diameter), corresponding to the region with dense GFAP+ Müller Cells (Fig. 4*B*), did not show any clear light response by 21 d. Remarkably, the outer portion of the injury field (excluding inner ∼40 μm) had mostly recovered function, with backscattering changes whose kinetics and magnitudes nearly matched that of the control region (Fig. 5 *C* and *D*).

Temporal Dynamics of Injury, Microglial Response, Tissue Remodeling, and Recovery of Function. To examine the temporal relationship between the recovery of photoreceptor function within the injury field and the microglial response to injury, we compared the extent of photoreceptor damage (OCT intensity at damage, Fig. 6*A*), microglia density (SLO GFP intensity, Fig. 6*B*), and photoreceptor function (optophysiology response, Fig. 6*C*) over time and averaged the results across animals ($n = 4$ animals, 8 retinas for injury and response field analysis; 5 animals, 5 retinas for optophysiology analysis). As described for the representative example in Fig. 5, over the first 24 h after damage there was an immediate increase in baseline light scattering (Fig. 6*A*) and loss of photoreceptor response to 488-nm light (Fig. 6*C*), consistent with photoreceptor damage. Surprisingly, on days 2 and 3, the bleach-driven response showed a slight improvement that coincided with microglia migration into the damage field (Fig. 6 *B* and *C*). By 7 d the injury field again showed minimal functional response (Fig. 6*C*), at a time coinciding with the microglia returning to their normal positions (Fig. 6*B*), and thus may reflect the completion of phagocytosis of photoreceptors that had retained some function, which was regained as the initial stress due to the light exposure abated. Over a much longer time scale, function then continued to improve, until by 21 d the magnitude of the bleach-driven response within the injury field recovered to 80% the magnitude of the control field well outside the damaged area. Homozygous *Cx3CR1*$^{GFP/GFP}$ mice had a very similar pattern of both OCT scattering changes (*SI Appendix*, Fig. S6*A*) and microglial migration (*SI Appendix*, Fig. S6*B*), although by 21 d there was a small, sustained increase in both OCT backscatter and GFP fluorescence. Overall, these results reveal that functional recovery of a previously damaged neural tissue over a time scale of weeks is not concurrent with the microglial response. Rather, tissue remodeling and return of function takes place after damaged cells are cleared and the microglia have disappeared from the injury locus.

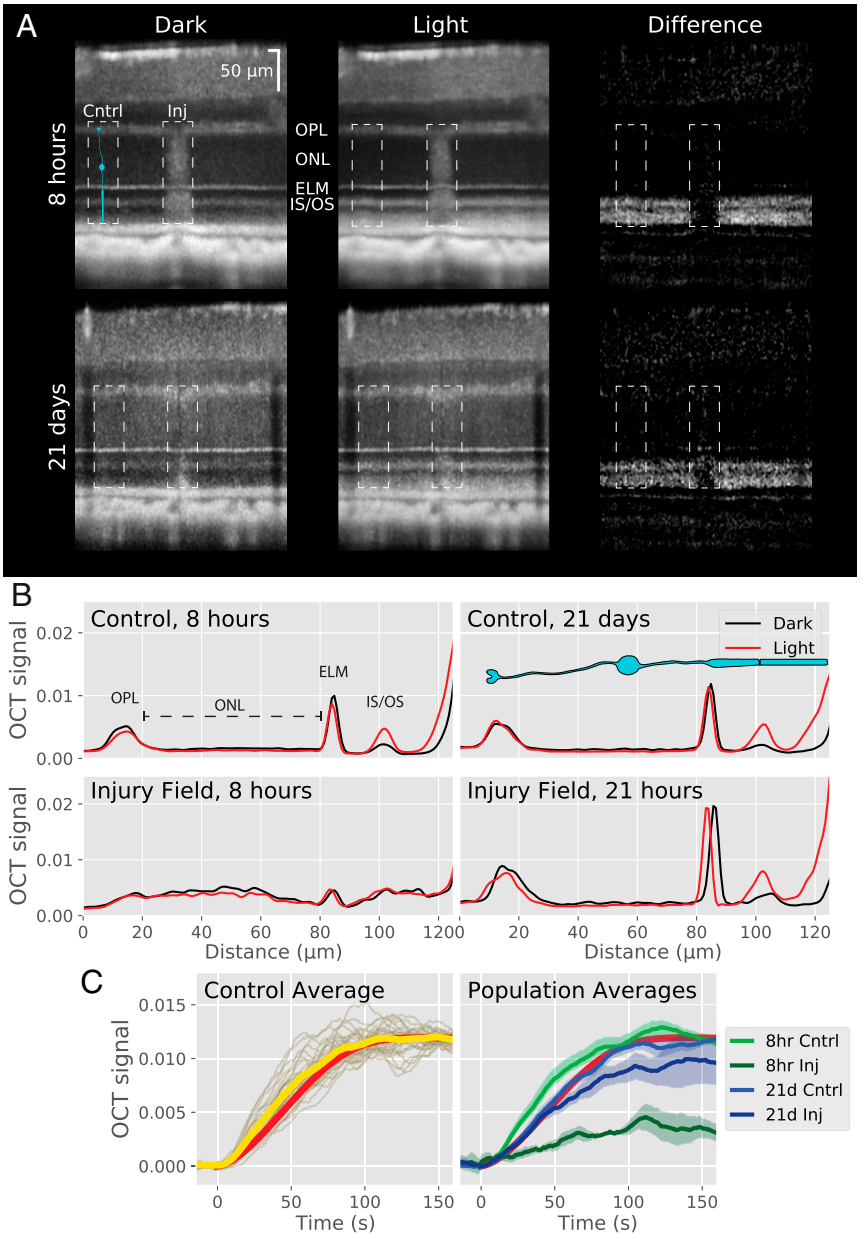

Fig. 5. Optophysiology reveals functional recovery of rod phototransduction at the injury locus. (*A*) Optophysiological responses of rods at 8 h and 21 d after focal injury. OCT B-scans through the injury locus taken in the dark-adapted state (Dark) and 150 s after bleaching 10% of the rhodopsin (Light) have been subtracted (Difference) to reveal pronounced changes in scattering induced by phototransduction (30). At 8 h, bleaching increased scattering at the IS/OS boundary and photoreceptor tips outside the injury field (Cntrl dashed box), but not within in the injury field (Inj box). The bleaching-induced light scattering in this region improved by 21 d. (*B*) Quantification of the bleach-induced scattering changes revealed by averaging the intensities of the B-scans in the control region and injury field in the dark-adapted state (black) and 150 s postbleaching (red). (*C*) Time courses of the bleach-induced OCT signals. The responses in the control field were very similar over time (*Left*, Control Average); each golden trace is an individual determination from every mouse at every timepoint ($n = 32$). The population average (yellow) is very similar to the theoretical curve (red) from Zhang et al. (30). The population average responses (*Right*, displayed as mean ± SEM, $n = 5$) were very poor within the injury field 8 h after damage, but by 21 d the responses in that same region had recovered to 80% of the control region.

Discussion

The eye is a natural window into the CNS, endowed with optics that not only allow the organism to see but also the experimenter to visualize cellular-level structure and to assess neuronal function noninvasively and longitudinally. In this investigation we have exploited this natural window into the mouse retina, using multimodal SLO/OCT imaging to visualize 3D structural and fluorescence changes at the same locus over hours, days, and weeks in response to a focal neuronal injury affecting ∼4,500 photoreceptors (Figs. 2–5). These results reveal the time course of the injury and subsequent tissue remodeling, the spatiotemporal dynamics of the population of responsive microglia, and the complete loss and recovery of photoreceptor function at the damage locus (Figs. 5 and 6).

Optical Characterization of the Injured Photoreceptors. The intrinsically high axial resolution (∼2 µm) of OCT and its exquisite sensitivity to backscatter (∼10^{-7} changes in reflectivity) allowed the small region of neuronal damage to be precisely defined and repeatedly probed over months (Fig. 2). The photoreceptor somata within the injury field underwent a nearly instantaneous increase in light scattering, which further increased over the first ∼24 h and then declined with a half-time of ∼5 d. Scattering by the mitochondrial-rich inner segment region followed a similar time course, but with a somewhat slower and less complete recovery. "Superaveraging" the OCT volumes (Fig. 3 and Movies S6–S10) revealed a pattern of scattering in the ONL that suggests an increase in the refractive index difference between the nuclei and perinuclear cytoplasm. Given that cell nuclei have a lower refractive index than cytoplasm (31), these results imply that the damage response of the photoreceptor cell bodies corresponds either to an increase in nuclear water volume (which would further decrease its refractive index) and/or an increase in scattering elements in the perinuclear cytoplasm, possibly due to a large increase in thermally mediated aggregation of proteins and increase in dense, scattering organelles like lysosomes or stress granules. The use of OCT to probe changes in the cell body in this manner may be a valuable addition to the tool kit of in vivo assessment of neuronal cell health.

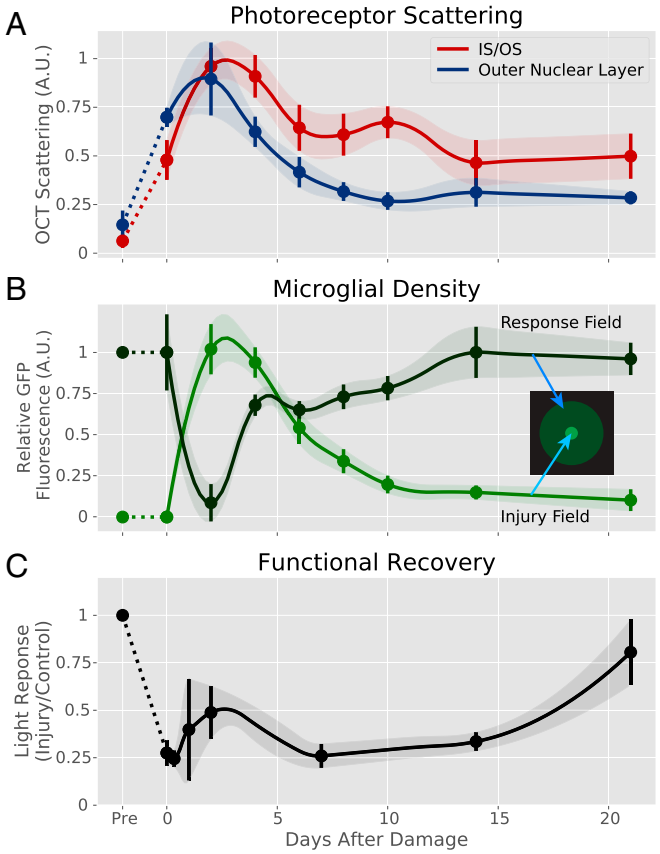

Fig. 6. Comparison of the time courses of photoreceptor layer injury and remodeling, microglial response, and functional recovery over 3 wk. (*A*) OCT scattering intensity changes in the ONL (blue symbols and line) and the inner and outer segments (IS/OS; red symbols and line) increased immediately after laser exposure and peaked in 2 d, after which recovery occurred over weeks. (*B*) The peak GFP fluorescence at the injury field (lighter green symbols and line) matched the timing of the peak in the OCT scattering in *A*. In contrast, GFP fluorescence declined in the response field surrounding the injury locus (darker green symbols and lines; see inset), consistent with lateral migration of microglia into the injury field from the surrounding response field. Both the injury field and surrounding response field recovered back to baseline levels over approximately 2 wk. Error bars are 1 SEM from 8 replications. (*C*) Recovery of rod phototransduction in the injury locus gauged by the amplitude of the optophysiological response had a time course distinct from that of the microglial response and commenced at about 10 d, when the microglia had largely returned to their baseline distribution (see *B*). Error bars are 1 SEM from 5 replications.

Extent of Microglial Dynamics and Activation Signals. Microglia showed no change in morphology or location for 1 h after the focal injury but within 8 h exhibited substantial polarization and somatic migration toward the injury locus, reaching a maximal density at the damage site in 2 d (Figs. 2 and 6*B*). This time scale of somatic migration is very similar to those reported in in vivo imaging studies in the brain (32–34) (e.g., see Movie 2 in ref. 32) and retina (10), all of which required >6 h for measurable somatic movement toward a focal injury. Nonetheless, other in vivo imaging studies have seen more extensive and rapid microglial processes motility in both the brain (32, 33, 35, 36) and the retina (17), which may have been undetectable in our SLO imaging system because its z-resolution is less than those of the 2-photon and AO time-lapse imaging used in the previous work. Interestingly, we did observe atypical (nonramified) GFP+ cells with high process motility (*SI Appendix*, Fig. S2 and Movie S3). These active cells constituted a rare subset (~5% of GFP+ cells), underscoring the value of wide-field imaging for ensuring adequate sampling of the GFP+ population.

Photodamage is always a concern in imaging experiments, but it is unlikely that the extent and timing of the microglia response in our studies was affected by photolytic damage because the 488-nm laser power used for microglial imaging (100 μW) was similar to or lower than that used in previous retinal microglial imaging studies (e.g., 100 to 230 μW in ref. 17). Given the areas of our scan fields and duration of exposure, we estimate that each of our typical 10-min small-field SLO imaging sessions resulted in a cumulative radiant exposure of no more than 14 J·cm^{-2}. Although safety standards have not been established for mice, when converted to retinal energy density the exposure falls 0.09 $\log_{10}$ units below the human American National Standards Institute standard exposure limit, which itself is defined to be 10-fold lower than the energy density that causes retinal damage 50% of the time.

The microglial response that we measured was not affected by the "calming" influence of Cx3CL1-Cx3CR1 signaling (4, 37, 38). Although *Cx3CR1*$^{GFP/GFP}$ microglia show slower (−38%) cell migration rates than *Cx3CR1*$^{+/GFP}$ mice ex vivo (39), we could detect no such effect on the time course of formation or resolution of the microglia clusters in our study (compare Fig. 6 *A* and *B* to *SI Appendix*, Fig. S6). Notably, the ex vivo study measured these morphological changes on the time scales of minutes, while the present work examined microglial densities between strains over days and weeks. Whatever the nature of the chemotactic activation signal in our study, it is clearly determined by something other than Cx3CR1 signaling.

Retinal Remodeling and Recovery of Function after Neuronal Injury. Our multimodal imaging of neurons and microglia over weeks after injury revealed three distinct stages of tissue remodeling: the restoration of the microglial population to its preinjury distribution and stellate form (Figs. 2, 4, and 6*B*), the remodeling of the photoreceptor layer at the injury locus (Figs. 2 and 6*A* and Movie S10), and the recovery of phototransduction in the injury field (Figs. 5 and 6*C*). It is not yet clear whether most photoreceptors in the injury zone die and are cleared or survive and recover function. However, the loss of photoreceptors in the injury field (Fig. 4*A*) and engulfment of the injured cells by microglia (Fig. 4*B* and *SI Appendix*, Fig. S5) suggest that the microglia are phagocytosing dying cells. The reestablishment of normal distribution and morphology of microglia by 7 d after injury (Figs. 2 and 4*B*) implies that by 7 d the microglial-activating signals have dissipated and the signal(s) responsible for normal maintenance of microglial tiling again returned to dominance over those driving morphological change and movement. Moreover, remodeling of the distribution of cell bodies in the ONL and the restoration of rod function take place after the microglia mosaic has returned to normal (Figs. 2, 4, and 6 *B* and *C*). This delay in remodeling that suggests that functional recovery involves slow spatial rearrangements of photoreceptors into space created by phagocytosed cells, or reconstruction of the outer segments of surviving photoreceptors from that original locale, which should take about 10 d based on the rate of normal outer segment renewal (Fig. 6*C*). It remains an important open question whether recovery of photoreceptor function translates into visual function. After local laser ablation, the photoreceptor mosaic redistributes to fill in the vacated space left by the lost cells in rabbits (40), rats (41), macaques (25, 42), and humans (43). Furthermore, there are reports that bipolar cells and ganglion cells that were previously connected to the lost photoreceptors may be able to make new circuits with the migratory cells (44, 45). These results suggest a conserved mechanism for functional recovery after local damage in the mammalian retina.

Future Directions and Applications for Longitudinal, Multimodal Retinal Imaging. The local light damage model employed here provides a reliable framework for investigating the dynamics of retinal remodeling at the level of single cells. Future experiments that allow individual microglia to be tracked within the field of many should help to reveal the fate of individual cells once they have migrated into the cluster. Are the microglia that migrated the same cells that are seen engulfing photoreceptor nuclei? Do those cells phagocytose or merely provide neurotrophic support and then release the same photoreceptors? Do the microglia die, or do they migrate out of the injury field? The extent to which migration, proliferation, or cell death participate in reestablishing the microglia mosaic is an important focus for subsequent investigations.

This model also holds the potential to identify the time- and distance-varying signals that cause cells to cluster at the damage locus transiently and those that underlie restoration of the mosaic spatial distribution. In other models where photoreceptors die, microglia respond first, and monocytes subsequently infiltrate over the following days [e.g., Karlen et al. (46) and Ma et al. (47)]. Although infiltrating monocytes are morphologically and molecularly distinct from microglia initially, they can differentiate into microglia-like macrophages within the retina [e.g., O'Koren et al. (48), Paschalis et al. (49), and Ronning et al. (50)]. It is possible that in our experiments bone marrow-derived cells also infiltrate and participate in the engulfment of photoreceptors and/or the repopulation of the *Cx3CR1*$^{+/GFP}$ cell mosaic.

In future work, introduction of cell-type-specific fluorescent optogenetic reporters into other relevant cell types, including rods, Müller glia, and bipolar cells, will enable detection of individual cell–cell interactions in vivo with AO-SLO, while refined analysis with AO-OCT may reveal the fate of individual rods and other cells (29). These multimodal imaging methods will allow closer examination of the mechanisms of the functional photoreceptor recovery in vivo and how the retinal circuitry downstream of the affected photoreceptors may likewise adapt. Thus, the work presented here lays a rigorous foundation for in vivo identification of the molecular signals and cellular processes involved in the microglial response to neuronal injury in the CNS and the roles of immune signaling and glial cells in subsequent tissue remodeling.

Methods

Animals. All animals were cared for and handled in accordance with National Institutes of Health Guidelines for the care and use of experimental animals and protocols approved by the Institutional Animal Care and Use Committee of the University of California, Davis. Homozygous *Cx3CR1*$^{GFP/GFP}$ knock-in mice (51) were obtained from The Jackson Laboratory (strain 005582) and outbred to c57Bl/6J mice to obtain *Cx3CR1*$^{+/GFP}$ heterozygotes. For imaging, mice were anesthetized with 2 to 2.5% isoflurane and positioned on a heating pad (37 °C) with a rectal feedback probe (TCAT-2LV; Physitemp). Maintaining the mouse at body temperature was imperative for the light damage to occur. The heating pad was mounted on a 3D-printed stage to connect a bite bar (923-B Mouse Gas Anesthesia Head Holder; Kopf) with a micropositioner (Bioptigen) that allowed rotational and translational adjustment for positioning the mouse with respect to the contact lens, while preventing large breathing artifacts in the images. The pupils were dilated and cyclopleged with tropicamide and phenylephrine, and the corneal surface wetted with hypromellose gel (GenTeal Tears Severe; Alcon). The artificial tears helped to maintain a homogeneous refractive surface between the cornea and the custom 0 diopter contact lens (Unicon Corporation). After each imaging session, which typically lasted 10 to 30 min, the mice were returned to their cages where they became fully ambulatory within ∼10 min and for the remainder of the time until the next imaging session commenced.

Equipment and Settings.

In vivo imaging. A custom-built multimodal SLO and OCT system was used to image GFP+ cells within the context of the retinal tissue using two simultaneously acquired channels, fluorescence and reflectance. The SLO channel (488-nm excitation wavelength, 100 μW at pupil) was used to image GFP fluorescence (2-Hz frame rate, 256 × 256 pixels) while the OCT channel was used to monitor the acute changes in light scattering induced by infrared light exposure (52, 53). All images are of *Cx3CR1*$^{+/GFP}$ mice unless otherwise noted.

The wide-field images were acquired over 51° visual angle (2,193 μm) with a lateral resolution of ∼3 μm (52). Increased digital sampling was used to "zoom" in on the population of cells in the injury field, 728 × 728 μm. The FD-OCT system collects interferometric spectral fringe pattern that is produced by combining light back-scattered from the sample (mouse retina) and from the reference arm. These data are then processed using standard OCT data processing methods to reconstruct intensity of back-scattered light as a function of depth (54). To convert visual angle to retinal distance, we used the conversion factor of 43 μm per degree of visual angle, which was obtained by comparing the SLO images of the vasculature with live ex vivo confocal images of the same flat-mounted retina (55). This is close to, but somewhat different from, the established conversion factor of 34 μm per degree of visual angle, a difference attributable to the use of the custom contact lens (6, 20, 53, 56)

The OCT light source was a superluminescent diode with a 132-nm bandwidth centered at 860 nm (Broadlighter T-860-HP; Superlum). The power for scanning was 600 μW measured at the mouse pupil. For inducing damage, this laser was parked at a single location at full power (8 mW measured at the pupil) for 120 s. This caused the scattering increase in a circle with a diameter of ∼150 μm. Exposures shorter in duration than 120 s did not consistently cause damage. Damage was most commonly induced in the dorsal retina for technical ease, but we also induced injury in other retinal locations and did not observe any variation in the extent of damage, the microglial response, or the recovery process.

A separate, custom-built adaptive-optics scanning laser ophthalmoscope [AO-SLO (6)] was used to image fluorescent microglia in retinas with axial resolution needed to resolve their depth localization. Fluorescent images driven by a 488-nm solid-state laser (100 μW at the pupil) were acquired at 5 Hz for a 400- × 400-pixel sampling density frame over a retinal area of 301 × 301 μm. We did not look at process motility with AO-SLO.

There are two independent ways to shift the focus plane of the AO system to different retina layers: One is adding defocus onto the wavefront sensor reference that forces the deformable mirror to move focus; the other one is to freeze the AO system and vary the gel thickness between the contact lens and the mouse cornea (56). The latter method was easier to use for searching the region of interest, while the first method was used for precise control of the location of the focal plane. The NFL layer was identified by the nerve fiber bundles, and the IPL and OPL were distinguished by the retinal capillaries using the blue light reflectance image to locate the specific layers of the retina to axial position of corresponding microglia cells.

Image processing. Image processing was performed using the Fiji version of ImageJ (56) and the Scikit-Image Python package (58).

There was often some drift of the eye position over longer imaging periods. Misaligned frames were registered with the TurboReg Plugin (59) or the modified version, MultiStackReg, written by Brad Busse. A stack of images was typically registered with a rigid body transformation. Occasionally, rigid body registration would produce a suboptimal image and a translation-only transformation was used instead. All images in a stack were registered with the first image in the series. Final images were produced by taking the median image of the remaining frames, of which there were typically about 50 frames for widefield and about 200 frames for zoomed images. For assessing motility, curated time-series image stacks over 10 min were grouped and the median images of each group used for analysis and presentation. Time-coded color projection images were made by taking the median of a grouped set of images and colorizing them as a function of time using the Temporal Color Code macro (with a custom LUT) for ImageJ written by Kota Miura (available with Fiji), modified to produce either the SD or maximum intensity projection image. Due to condensation on the corneal lens over longer imaging sessions, in some sets of images there was a decrease in intensity. This was corrected using the total image intensity to normalize all images in each set to the same mean intensity. This function was carried out by the Bleach Correction macro written by Jens Reitdorf (https://www.embl.de/eamnet/html/bleach_correction.html).

For each set of SLO images, an OCT volume was also acquired. We used standard OCT data processing steps to generate a series of OCT B-scans. Retinal layers in B-scans were flattened with a custom Python script that employed a strip registration algorithm, whereby each A-scan was cross-correlated to the middle A-scan in the image to detect the vertical displacement. After each B-scan was flattened, the middle A-scan was used to detect vertical displacement between B-scans. Each B-scan was then shifted to produce a flattened OCT volume.

Analysis of Microglial Density. To quantify the distribution of microglia in the retina, mice were aligned with the optic nerve head (ONH) at each four sides of the square imaging field, yielding images that encompassed up to 51° of the 4 quadrants of the retina for each mouse. Cell locations and numbers were estimated with the Image-based Tool for Counting Nuclei (ITCN) plugin for ImageJ, which uses an inverted Laplacian of Gaussian filter and local maxima detection for nuclear localization (60). The output of the ITCN plugin highlights the locations of detected cells for independent validation by visual inspection. To determine the location of microglia with respect to the ONH, the retina was assumed to be the surface area of hemisphere with a radius of 1,650 μm (61, 62). The center of the ONH was manually determined for each image and the angular coordinates (arc length and azimuthal angle) of microglia were calculated. To ensure that cells were not double-counted, cells in each image that were outside the 90° field that defined the quadrant of the image were not considered. Dorsal was defined as 315 to 45°, with angle increasing counterclockwise (*SI Appendix*, Fig. S1*D*), and posterior was defined as 45 to 135°. The density of cells was calculated in bins of 1° for the azimuthal distribution or 50 μm in arc length for the radial distribution.

OCT and SLO Image Analysis. To locate and measure the scattering changes that occurred in the OCT images after damage, the two brightest peaks of the average A-scan, which correspond to the RPE and choroid, were used as a reference to isolate the photoreceptor layer from the OCT image, based on the photoreceptor layer thickness of ∼100 μm (21). The variance projection image of the photoreceptor layer in depth was used to get an *en face* image, where the damage spot would be very bright against the surrounding healthy tissue and was used to find the rough location of the damaged area. The location was then refined by taking the local region around the damage and segmenting with Yen thresholding (63). The accurate location of the damage was determined by taking the centroid of the resulting object. This was used as the center point for the annular analysis used to quantify the scattering profile. If the centroid could not be detected, the image was rejected from the dataset. Rings of ∼9 μm thickness [1 pixel, using Andres' method (64)] were taken outward from the centroid, and the intensity in each was averaged. The background was calculated as the average intensity from rings with radius ∼250 to 500 μm and the intensity profile from 0 to 175 μm was background-subtracted to normalize for intensity differences between images. This was done for the IS/OS and the ONL, which were a consistent distance from the RPE, allowing them to be reliably segmented from the OCT datasets. All structural OCT analysis was done on volumes where the scattering intensity was logarithmically transformed.

The same annular analysis was then done for the simultaneously captured fluorescence SLO images to quantify the microglial response. The centroid location from the OCT image was taken and used as the location for the SLO image. Intensity was used as a measure for microglia because cells within the cluster could not be reliably discerned to determine the density.

Plots were made using matplotlib for Python (65). Statistical tests were done with Scipy, using an *F* test, when appropriate, and Student's *t* test. Throughout, error bars indicate the SEM.

Superaveraging OCT. Following the methods of Liu et al. (29), we captured 60 OCT volumes, 728 μm × 728 μm. Each corresponding B-scan of an individual volume scan was registered with MultiStackReg, using a Rigid Body transformation, and the registered volumes were then averaged. For presentation, both B-scans and segmented enface ONL volumes were background-subtracted and contrast-enhanced.

Optophysiological OCT. Following the methods of Zhang et al. (30), C57Bl6/J mice were dark-adapted for at least 8 h. Mice were aligned across multiple sessions with *en face* imaging of the retinal vascular map obtained with nonstimulating NIR OCT. Once the injury field was located, scan parameters were set so that 8 successive B-scans would capture the entire injury field as well as distant, undamaged retina that served for control. OCT B-scans were captured for ∼15 s before light exposure. A 488 nm, 10-μW light was then scanned across the imaged region once to bleach a 10% of the rhodopsin (55). The region was then repeatedly imaged with OCT for ∼250 s to capture the rod optophysiological response.

To analyze, B-scans that did not include the injury field were removed and the remaining B-scans were registered and averaged and flattened to produce a single B-scan for each time step. Once flattened, a control region 120 μm wide was chosen based on vascular landmarks that were consistently used for the entire 3-wk experiment. The B-scans of the injury field were analyzed into two portions: shell (periphery) and core. The core was ∼40 μm in diameter and contained scarring that did not disappear over 1 mo. The shell comprised the damaged region flanking the core on each side. Because the core did not show recovery, it was not included in the analysis. There were light-evoked backscattering changes in both the IS/OS and rod tips and the IS/OS region was chosen for analysis based on previous work proposing a mechanism responsible for the changes (30). The intensity in the IS/OS at each time point was averaged in the control region and the shell to extract the optophysiological response triggered by the 488-nm light exposure. There was some variation of the amount of backscatter in the dark and the magnitude of the light response between each time point and each animal. To account for this, the intensity of the control IS/OS in the dark was used to background-subtract the control and damage light responses. The control magnitudes were then all scaled to the same average value between 136 and 182 s after light exposure. The appropriate scale factor was then used to adjust the magnitude of the response of the damage region. Responses were then averaged across mice for each time point. The control responses in Fig. 5 were then boxcar-filtered for presentation. To summarize the changes during recovery, the magnitude of the optophysiological response was determined by comparing the IS/OS intensity difference between peak light response and the dark-adapted state. The size of the response in the shell was then normalized to the response in the control region. Eq. **1** describes the results in Fig. 6*C*, where *IF* is injury field and corresponds to the shell and *CR* is control region:

$$Response\ Magnitude = \frac{Light_{IF} - Dark_{IF}}{Light_{CR} - Dark_{CR}}. \quad [1]$$

Histology. Flat-mounted retinas were prepared following the method of Ronning et al. (66). In short, mice were killed with CO_2 narcosis and eyes removed and submerged in 4% paraformaldehyde for 20 min. Retinas were mounted photoreceptor side up and stained with DAPI (Invitrogen) and antibodies against CD11b (Biolegend 101218, 1:300) for microglia and GFAP (Dako X0334, 1:1,000) for reactive Müller glia. Retinas were then imaged using a Nikon A1 microscope.

For toluidine blue-stained sections, mice were asphyxiated with CO_2 and cardiac-perfused with 2% paraformaldehyde and 2.5% glutaraldehyde in 0.1 M sodium cacodylate buffer. The eyes were enucleated, rinsed with 0.1 M sodium cacodylate buffer, treated with 2% osmium tetroxide, and dehydrated in ethanol. Eyes were then embedded in Poly/Bed 812 resin. Embedded retinas were then sectioned with an EMUC6 μLtramicrotome at 1.5 μm with a glass knife. Every 20th section was collected and stained with toluidine blue.

ACKNOWLEDGMENTS. We thank Dr. Sarah J. Karlen and Kaitryn Ronning for helpful discussions and technical assistance and Brad Shibata for help with histology. This work was supported by the National Institutes of Health (R01-EY24320, T32-GM007377, T32-EY105387, and P30-EY012576).

1. H. Kettenmann, F. Kirchhoff, A. Verkhratsky, Microglia: New roles for the synaptic stripper. *Neuron* **77**, 10–18 (2013).
2. A. Sierra, M.-È. Tremblay, H. Wake, Never-resting microglia: Physiological roles in the healthy brain and pathological implications. *Front. Cell. Neurosci.* **8**, 240 (2014).
3. G. C. Brown, J. J. Neher, Eaten alive! Cell death by primary phagocytosis: 'Phagoptosis'. *Trends Biochem. Sci.* **37**, 325–332 (2012).
4. Y. Wolf, S. Yona, K.-W. Kim, S. Jung, Microglia, seen from the CX3CR1 angle. *Front. Cell. Neurosci.* **7**, 26 (2013).
5. Q. Li, B. A. Barres, Microglia and macrophages in brain homeostasis and disease. *Nat. Rev. Immunol.* **18**, 225–242 (2018).
6. R. J. Zawadzki *et al.*, Adaptive-optics SLO imaging combined with widefield OCT and SLO enables precise 3D localization of fluorescent cells in the mouse retina. *Biomed. Opt. Express* **6**, 2191–2210 (2015).
7. C. Alt, J. M. Runnels, G. S. L. Teo, C. P. Lin, In vivo tracking of hematopoietic cells in the retina of chimeric mice with a scanning laser ophthalmoscope. *IntraVital* **1**, 132–140 (2015).
8. A. Bosco, C. O. Romero, B. K. Ambati, M. L. Vetter, In vivo dynamics of retinal microglial activation during neurodegeneration: Confocal ophthalmoscopic imaging and cell morphometry in mouse glaucoma. *J. Vis. Exp.*, e52731 (2015).
9. B. M. Davis, M. Salinas-Navarro, M. F. Cordeiro, L. Moons, L. De Groef, Characterizing microglia activation: A spatial statistics approach to maximize information extraction. *Sci. Rep.* **7**, 1576 (2017).
10. C. Alt, C. P. Lin, "In vivo quantification of microglia dynamics with a scanning laser ophthalmoscope in a mouse model of focal laser injury" in *Proceedings of SPIE* (SPIE, Bellingham, WA, **vol. 8209**, 2012), pp. 820907–820909.
11. C. Alt, J. M. Runnels, L. J. Mortensen, W. Zaher, C. P. Lin, In vivo imaging of microglia turnover in the mouse retina after ionizing radiation and dexamethasone treatment. *Invest. Ophthalmol. Vis. Sci.* **55**, 5314–5319 (2014).
12. S. Crespo-Garcia *et al.*, In vivo analysis of the time and spatial activation pattern of microglia in the retina following laser-induced choroidal neovascularization. *Exp. Eye Res.* **139**, 13–21 (2015).

13. N. Eter *et al*., In vivo visualization of dendritic cells, macrophages, and microglial cells responding to laser-induced damage in the fundus of the eye. *Invest. Ophthalmol. Vis. Sci.* **49**, 3649–3658 (2008).
14. S. Joly *et al*., Cooperative phagocytes: Resident microglia and bone marrow immigrants remove dead photoreceptors in retinal lesions. *Am. J. Pathol.* **174**, 2310–2323 (2009).
15. J. E. Lee, K. J. Liang, R. N. Fariss, W. T. Wong, Ex vivo dynamic imaging of retinal microglia using time-lapse confocal microscopy. *Invest. Ophthalmol. Vis. Sci.* **49**, 4169–4176 (2008).
16. M. Paques *et al*., In vivo observation of the locomotion of microglial cells in the retina. *Glia* **58**, 1663–1668 (2010).
17. D. J. Wahl, R. Ng, M. J. Ju, Y. Jian, M. V. Sarunic, Sensorless adaptive optics multimodal en-face small animal retinal imaging. *Biomed. Opt. Express* **10**, 252–267 (2018).
18. S. Liu *et al*., Tracking retinal microgliosis in models of retinal ganglion cell damage. *Invest. Ophthalmol. Vis. Sci.* **53**, 6254–6262 (2012).
19. A. I. Jobling *et al*., The role of the microglial Cx3cr1 pathway in the postnatal maturation of retinal photoreceptors. *J. Neurosci.* **38**, 4708–4723 (2018).
20. Y. Geng *et al*., Adaptive optics retinal imaging in the living mouse eye. *Biomed. Opt. Express* **3**, 715–734 (2012).
21. L. R. Ferguson, J. M. Dominguez, 2nd, S. Balaiya, S. Grover, K. V. Chalam, Retinal thickness normative data in wild-type mice using customized miniature SD-OCT. *PLoS One* **8**, e67265 (2013).
22. X. Wang *et al*., Requirement for microglia for the maintenance of synaptic function and integrity in the mature retina. *J. Neurosci.* **36**, 2827–2842 (2016).
23. E. S. Levine *et al*., Rapid light-induced activation of retinal microglia in mice lacking Arrestin-1. *Vision Res.* **102**, 71–79 (2014).
24. R. Tanabu *et al*., The findings of optical coherence tomography of retinal degeneration in relation to the morphological and electroretinographic features in RPE65-/- mice. *PLoS One* **14**, e0210439 (2019).
25. J. M. Strazzeri *et al*., Focal damage to macaque photoreceptors produces persistent visual loss. *Exp. Eye Res.* **119**, 88–96 (2014).
26. S. G. Jacobson *et al*., Disease boundaries in the retina of patients with Usher syndrome caused by MYO7A gene mutations. *Invest. Ophthalmol. Vis. Sci.* **50**, 1886–1894 (2009).
27. N. Monai *et al*., Characterization of photoreceptor degeneration in the rhodopsin P23H transgenic rat line 2 using optical coherence tomography. *PLoS One* **13**, e0193778 (2018).
28. V. J. Srinivasan *et al*., Multiparametric, longitudinal optical coherence tomography imaging reveals acute injury and chronic recovery in experimental ischemic stroke. *PLoS One* **8**, e71478 (2013).
29. Z. Liu, K. Kurokawa, F. Zhang, J. J. Lee, D. T. Miller, Imaging and quantifying ganglion cells and other transparent neurons in the living human retina. *Proc. Natl. Acad. Sci. U.S.A.* **114**, 12803–12808 (2017).
30. P. Zhang *et al*., In vivo optophysiology reveals that G-protein activation triggers osmotic swelling and increased light scattering of rod photoreceptors. *Proc. Natl. Acad. Sci. U.S.A.* **114**, E2937–E2946 (2017).
31. M. Schürmann, J. Scholze, P. Müller, J. Guck, C. J. Chan, Cell nuclei have lower refractive index and mass density than cytoplasm. *J. Biophotonics* **9**, 1068–1076 (2016).
32. D. Davalos *et al*., ATP mediates rapid microglial response to local brain injury in vivo. *Nat. Neurosci.* **8**, 752–758 (2005).
33. A. Nimmerjahn, F. Kirchhoff, F. Helmchen, Resting microglial cells are highly dynamic surveillants of brain parenchyma in vivo. *Science* **308**, 1314–1318 (2005).
34. T. D. Y. Kozai, A. L. Vazquez, C. L. Weaver, S.-G. Kim, X. T. Cui, In vivo two-photon microscopy reveals immediate microglial reaction to implantation of microelectrode through extension of processes. *J. Neural Eng.* **9**, 066001 (2012).
35. H. Wake, A. J. Moorhouse, S. Jinno, S. Kohsaka, J. Nabekura, Resting microglia directly monitor the functional state of synapses in vivo and determine the fate of ischemic terminals. *J. Neurosci.* **29**, 3974–3980 (2009).
36. J.-H. Park, L. Kong, Y. Zhou, M. Cui, Large-field-of-view imaging by multi-pupil adaptive optics. *Nat. Methods* **14**, 581–583 (2017).
37. Y. Zhang *et al*., Repopulating retinal microglia restore endogenous organization and function under CX3CL1-CX3CR1 regulation. *Sci. Adv.* **4**, eaap8492 (2018).
38. M. K. Zabel *et al*., Microglial phagocytosis and activation underlying photoreceptor degeneration is regulated by CX3CL1-CX3CR1 signaling in a mouse model of retinitis pigmentosa. *Glia* **64**, 1479–1491 (2016).
39. K. J. Liang *et al*., Regulation of dynamic behavior of retinal microglia by CX3CR1 signaling. *Invest. Ophthalmol. Vis. Sci.* **50**, 4444–4451 (2009).
40. Y. M. Paulus *et al*., Healing of retinal photocoagulation lesions. *Invest. Ophthalmol. Vis. Sci.* **49**, 5540–5545 (2008).
41. E.-M. Busch, T. G. M. F. Gorgels, D. Van Norren, Filling-in after focal loss of photoreceptors in rat retina. *Exp. Eye Res.* **68**, 485–492 (1999).
42. C. Schwarz *et al*., Selective S cone damage and retinal remodeling following intense ultrashort pulse laser exposures in the near-infrared. *Invest. Ophthalmol. Vis. Sci.* **59**, 5973–5984 (2018).
43. D. Lavinsky *et al*., Restoration of retinal morphology and residual scarring after photocoagulation. *Acta Ophthalmol.* **91**, e315–e323 (2013).
44. A. Sher *et al*., Restoration of retinal structure and function after selective photocoagulation. *J. Neurosci.* **33**, 6800–6808 (2013).
45. C. Beier *et al*., Deafferented adult rod bipolar cells create new synapses with photoreceptors to restore vision. *J. Neurosci.* **37**, 4635–4644 (2017).
46. S. J. Karlen *et al*., Monocyte infiltration rather than microglia proliferation dominates the early immune response to rapid photoreceptor degeneration. *J. Neuroinflammation* **15**, 344 (2018).
47. W. Ma *et al*., Monocyte infiltration and proliferation reestablish myeloid cell homeostasis in the mouse retina following retinal pigment epithelial cell injury. *Sci. Rep.* **7**, 8433 (2017).
48. E. G. O'Koren, R. Mathew, D. R. Saban, Fate mapping reveals that microglia and recruited monocyte-derived macrophages are definitively distinguishable by phenotype in the retina. *Sci. Rep.* **6**, 20636 (2016).
49. E. I. Paschalis *et al*., Permanent neuroglial remodeling of the retina following infiltration of CSF1R inhibition-resistant peripheral monocytes. *Proc. Natl. Acad. Sci. U.S.A.* **115**, E11359–E11368 (2018).
50. K. E. Ronning, S. J. Karlen, E. B. Miller, M. E. Burns, Molecular profiling of resident and infiltrating mononuclear phagocytes during rapid adult retinal degeneration using single-cell RNA sequencing. *Sci. Rep.* **9**, 4858 (2019).
51. S. Jung *et al*., Analysis of fractalkine receptor CX(3)CR1 function by targeted deletion and green fluorescent protein reporter gene insertion. *Mol. Cell. Biol.* **20**, 4106–4114 (2000).
52. P. Zhang *et al*., In vivo wide-field multispectral scanning laser ophthalmoscopy-optical coherence tomography mouse retinal imager: Longitudinal imaging of ganglion cells, microglia, and Müller glia, and mapping of the mouse retinal and choroidal vasculature. *J. Biomed. Opt.* **20**, 126005 (2015).
53. P. Zhang, M. Goswami, A. Zam, E. N. Pugh, R. J. Zawadzki, Effect of scanning beam size on the lateral resolution of mouse retinal imaging with SLO. *Opt. Lett.* **40**, 5830–5833 (2015).
54. M. Wojtkowski *et al*., Ultrahigh-resolution, high-speed, Fourier domain optical coherence tomography and methods for dispersion compensation. *Opt. Express* **12**, 2404–2422 (2004).
55. P. Zhang, M. Goswami, R. J. Zawadzki, E. N. Pugh, Jr, The photosensitivity of rhodopsin bleaching and light-induced increases of fundus reflectance in mice measured in vivo with scanning laser ophthalmoscopy. *Invest. Ophthalmol. Vis. Sci.* **57**, 3650–3664 (2016).
56. P. Zhang *et al*., Effect of a contact lens on mouse retinal in vivo imaging: Effective focal length changes and monochromatic aberrations. *Exp. Eye Res.* **172**, 86–93 (2018).
57. J. Schindelin *et al*., Fiji: An open-source platform for biological-image analysis. *Nat. Methods* **9**, 676–682 (2012).
58. S. van der Walt *et al*.; scikit-image contributors, scikit-image: Image processing in Python. *PeerJ* **2**, e453 (2014).
59. P. Thévenaz, U. E. Ruttimann, M. Unser, A pyramid approach to subpixel registration based on intensity. *IEEE Trans. Image Process.* **7**, 27–41 (1998).
60. J. Byun *et al*., Automated tool for the detection of cell nuclei in digital microscopic images: Application to retinal images. *Mol. Vis.* **12**, 949–960 (2006).
61. A. L. Lyubarsky, L. L. Daniele, E. N. Pugh, Jr, From candelas to photoisomerizations in the mouse eye by rhodopsin bleaching in situ and the light-rearing dependence of the major components of the mouse ERG. *Vision Res.* **44**, 3235–3251 (2004).
62. S. Remtulla, P. E. Hallett, A schematic eye for the mouse, and comparisons with the rat. *Vision Res.* **25**, 21–31 (1985).
63. J. C. Yen, F. J. Chang, S. Chang, A new criterion for automatic multilevel thresholding. *IEEE Trans. Image Process.* **4**, 370–378 (1995).
64. E. Andres, Discrete circles, rings and spheres. *Comput. Graph.* **18**, 695–706 (1994).
65. J. D. Hunter, Matplotlib: A 2D graphics environment. *Comput. Sci. Eng.* **9**, 90–95 (2007).
66. K. E. Ronning *et al*., Loss of cone function without degeneration in a novel Gnat2 knock-out mouse. *Exp. Eye Res.* **171**, 111–118 (2018).